INTERNATIONAL JOURNAL OF AUTOMOTIVE AND MECHANICAL ENGINEERING (IJAME)
ISSN: 2229-8649 e-ISSN: 2180-1606
VOL. 19, ISSUE 4, 2022, 10132 – 10143
DOI: https://doi.org/10.15282/ijame.19.4.2022.10.0784

ORIGINAL ARTICLE

Numerical Investigation of Aerodynamic Characteristics of Hyperloop System Using Optimized Capsule Design

Prokash Chandra Roy, Arafater Rahman* and Mihir Ranjan Halder

Department of Mechanical Engineering, Khulna University of Engineering & Technology, Khulna-9203, Bangladesh

ABSTRACT – As a consequence of research on developing a speedy transportation system, Hyperloop is one of the best solutions now as smaller resistant forces are developed on the capsule body compared to conventional ground transportation systems due to movement in a vacuum and no contact with the ground. In this study, a capsule of an elliptical-shaped head and semicircular-shaped rear was chosen for analysis. Aerodynamic drags were calculated at different evacuated tunnel pressures. The computational regime was a 360 meters long tunnel. The inlet and outlet were pressure far-field boundaries while the wall was moving, with a Blockage Ratio (BR) of 0.36. Characteristics of different regions were identified in choked conditions. The drag was found to be lesser than the capsule of semicircular ends at different speeds. The pressure drag and friction drag were increased with the increase in velocity in the same tunnel pressure. By investigating different flow regions, it was found that a series of rhomboidal-shaped shock waves appear at high speeds. The formation and nature of this shock wave were also investigated, and found that it is caused due to shock wave and expansion wave interaction that results in the fall of pressure and temperature in the wake region.

ARTICLE HISTORY
Received: 14th June 2022
Revised: 20th Sept. 2022
Accepted: 21st Dec. 2022
Published: 3rd Jan. 2023

KEYWORDS
Hyperloop;
Blockage ratio;
Aerodynamic drag;
Choking;
Shock wave

NOMENCLATURE

L_{inflow}	length of the tube in front of the pod
L_{pod}	length of pod
L_{tube}	length of tube
D_{tube}	diameter of tube
D_{pod}	diameter of pod
M	Mach number
D_P	pressure drag
D_F	friction drag
D_T	total drag
P_{max}	maximum pressure
γ	molar heat capacity
BR	blockage ratio
A_{bypass}	bypass area
A_{tube}	tube area
ETT	evacuated tube transport

INTRODUCTION

The Hyperloop is considered to be the next-generation mode of transportation whose basic concept is similar to Oster's patented ETT system [1]. A standard train and a hyperloop system differ primarily in two ways. The hyperloop capsule is meant to float or levitate and propel itself using magnetic levitation or magnetically levitated high-speed capsules or pods that travel inside a partially evacuated tube. Likewise, compared to other existing transportation systems, the Hyperloop system offers advantages in terms of clean energy, speed, weather flexibility, and environmental impact, as the entire system is built to endure extreme weather and natural disaster-induced tremors. To ensure a sustainable environment, the hyperloop is powered by solar panels mounted on the tops of tunnels. The suspension of the hyperloop pod is supported by today's electromagnetic suspension system (EMS) [2] and the high-temperature superconducting suspension system (HTS) [3] to accelerate the high-speed scheme. Some businesses are racing to complete the commercialization of the Hyperloop system in this regard. Consequently, in November 2020, Virgin Hyperloop conducted the first passenger experiment where the track was 500 meters long, with a top speed of 387 kilometers per hour [4]. Elon Musk, an American engineer and entrepreneur, first published the concept of a hyperloop in a blueprint where the initial target speed is 1200 km/hr, which is over 1.5 times the speed of commercial jets [5]. To achieve this, the capsule is subjected to the least amount of air resistance and friction feasible. This enables the vehicle to reach higher

*CORRESPONDING AUTHOR | Arafater Rahman | ✉ arafat.refat1505060@gmail.com

speeds than a traditional high-speed train system. As a result, aerodynamic drag is a key factor to consider while developing a hyperloop better and faster future. Smaller drag reduces operational costs and the amount of power required to push the capsule. Following this, reducing aerodynamic drag has become a major research priority. Blockage ratio (BR), reduced air pressure, capsule head and tail shape, and pod velocity can all affect drag. In this regard, Niu et al. [6] used a transient numerical method to assess a three-dimensional train going through a tunnel where smaller blockage ratios and lower velocities compared to a hyperloop had aerodynamic repercussions on the tunnel wall's surface and rear effect on the surrounding objects. Zhang [7] also use the same method for a two-dimensional subsonic train going through the tube with varying pressure, velocity, and blockage ratios, but the shape of the capsule was arbitrary in this case. Again, the aerodynamic drag of transonic vehicles traveling through an evacuated tube was examined using the CFD method by Kang et al. [8]. Braun et al. [9] put a new dimension on this field by working on capsule shape and determined that the capsule's aerodynamics may be improved by a tunnel effect and the building of a low-drag capsule. Following this, Yang et al. [10]claimed that they found the best shape for the capsule's tail and head to minimize drag.

Among the numerous capsule front and rear designs, the one with an elliptical front and semicircular rear faces was shown to have the least drag. Afterward, Opgenoord et al. [11] investigated the effects of nose bluntness and tail height fluence on the aerodynamic drag of an axisymmetric pod by using a 3D Navier-Stokes CFD simulation. Nevertheless, Wong [12] also made an investigation on aerodynamic shape optimization using three different methods- inverse surface methods, inverse field methods, and numerical optimization methods. On contrary, the highest aerodynamic performance is possible when a pod's head and tail shape profiles are combined in a specific way [13]. Oh et al. [14] performed numerical analysis on a pod of the semi-spherical pod at different pressure, pod lengths, and temperatures and estimated the cost to overcome drag, where an axisymmetric steady model was used to simulate the flow regime. In addition to a flow regime, low Reynolds number compressible aerodynamics are numerically predicted by Desert et al. [15]. Capsule size consideration got important when Nick and Sato [16] used the Gamma transition model to determine aerodynamics and Fomin and Nalivaychenko [17] tried to estimate the range of possible values of drag force, possible values of lift force, and aerodynamic heating. Wave creation in high-speed transport is a common phenomenon [18]-[20]; following this, Le et al. [21] investigated the aerodynamic drag and pressure waves in different Hyperloop systems. Here a two-dimensional, axisymmetric, transient, dynamic mesh model was used to simulate waves formed by a high-speed pod moving inside a tunnel. The pod was semicircular on both ends. Kim et al. [22] simulate a hyperloop at various environmental conditions. They also found the critical speed at which the shock wave appears in the wake region.

A three-dimensional analysis of the effect of the nose and tail of five different shapes of the capsule at six different speeds was done by Le et al.[23]. Moreover, they found that symmetrically shaped capsule is lower than the other types, while aerodynamic lift varies drastically with the shapes. Yu et al. [24] recently investigated the choking mechanism with the corresponding physics and nature of the choked flow. According to this study, the intensity of choking increases with the acceleration of the capsule up to Mach 1, and then gradually diminishes with the elevation of the vehicle's speed. In addition, the relevant equation of choked condition was derived to benefit the design procedure of the Hyperloop system. A 3D study for shape optimization head and tail of a Hyperloop capsule was done by Kim and Oh [25] using a method called multi-resolution morphing by Kim and Oh [26] to enhance the aerodynamic performance of the system. This particular method is based on the artificial neural network (ANN). An optimal model of the capsule was found, the local flow characteristics were determined using this model, and the comparison of drag value was with the baseline model. Le et al. [27] did a transient study of the flow phenomena for multiple pods inside the evacuated tube and found that a connected capsule system produces lesser drag than an individual capsule system. This system actually resembles the actual condition with multiple capsules running in a system at the same time. A numerical simulation to determine the influence of Kantrowits limits on aerodynamic behavior was analyzed by Zhou et al. [28]. Here, two different blockage ratios (0.09 and 0.25) were taken. Furthermore, the impact of the length of the head and tail of the capsule on aerodynamic drag was also carried out. A transient numerical study was conducted by Jang et al. [29] for a capsule of semicircular ends. Pressure wave behaviour and aerodynamic drags were predicted in this study.

In a previous computational analysis, Oh et al. [14] estimated aerodynamic drags (total drag, pressure drag, and friction drag) for varying capsule speeds, capsule lengths, tunnel pressures, and blockage ratios (0.36, 0.25). In their experiment, a capsule with a semicircular head and tail was employed, but Yang et al. [10] found that the elliptical head and semicircle rear had the lowest pressure drag among six pairings of varied capsule head and rear geometries (linear-semicircular, linear-ellipse, linear-rectangular, linear-linear, semicircle-semicircular, ellipse-semicircular). So, an optimized shape capsule (elliptical head and semicircular rear) was used in our study; all other geometry and boundary conditions remained the same as Oh et al. [14]. Consequently, a comprehensive inspection utilizing a capsule with the optimal shape (elliptical head and semicircle rear) is required. Upon completion of the simulation, shock waves are generated in the wake zone at transonic speeds, and the drag increases dramatically. The focus of this study is on computing aerodynamic drag for an optimal capsule shape and explaining the shock wave observed at high speeds.

NUMERICAL METHOD

Computational Model

The simulation was conducted on ANSYS Fluent 18.1 (Ansys Inc., Canonsburg, PA, United States) with the shear stress transport (SST) k-ω viscous model. Using a stable, density-based, implicit solver, the compressible ideal gas condition was set. Sutherland's viscosity model was thought to describe viscosity. In this concept, viscosity is solely dependent on temperature. The Transition SST (4-equation) model was chosen for the turbulence model because it is

more accurate than the traditional SST k- (2-equation) model. Figure 1(a) depicts the computational domain and boundary conditions, where the entrance and outflow were chosen as pressure far-field boundaries such that no reflection could occur at the borders. Likewise, the tube wall was chosen to be a nonslip surface flowing at the same velocity as the flow velocity at the pressure far-field boundary. The capsule was chosen as a permanent wall. Figure 1(b) depicts the required system's dimensions. The diameter of the capsule or pod was 3 meters, while the diameter of the tube or tunnel was 5 meters. If the tube is too small, pressure waves may reflect from the tube's edges, resulting in erratic fluctuations in pressure. The length chosen for the tube was 360 m because the long tunnel has a positive influence on pressure waves, so the waves can develop to their maximum capacity without incurring losses or reflections [30], [31]. The temperature of 300 K was decided, and capsule speeds of 150 m/s, 200 m/s, 250 m/s, 300 m/s, and 350 m/s were considered throughout the tunnel to find the best feasible result. Nevertheless, for the pressure far-field boundary, the numbers of 0.4322, 0.5762, 0.7209, 0.8643, and 1.0084 were chosen as the Mach number. The inlet airflow pressures were set at 101.325 Pa, 500 Pa, and 1013.25 Pa. The nonslip tunnel walls moved at the same pace as distant pressure.

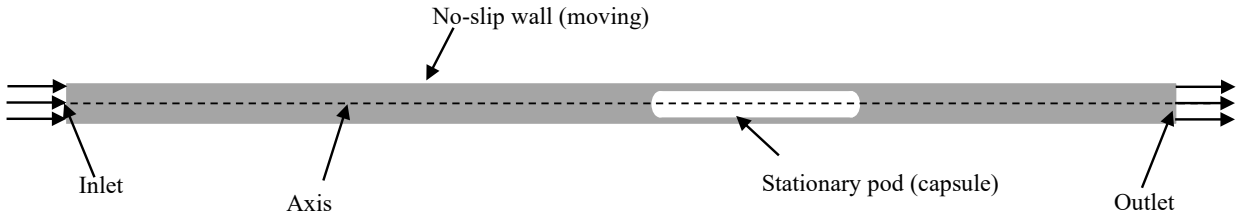

(a)

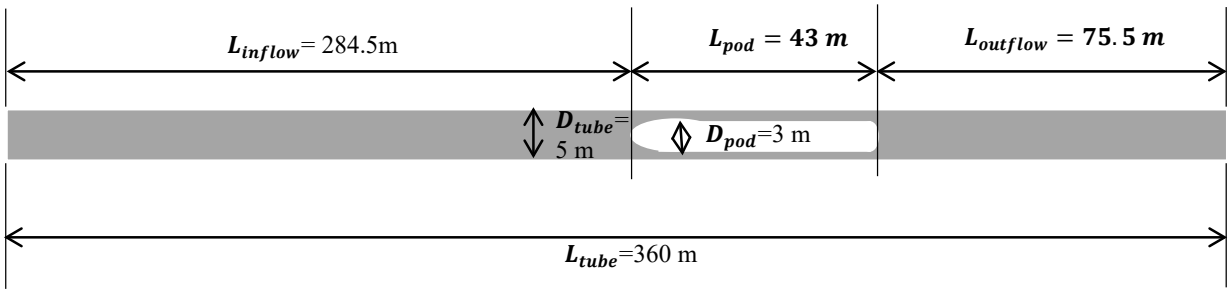

(b)

Figure 1. Schematic of the (a) computational model and boundary conditions and (b) dimensions of the model

The blockage ratio was determined to be 0.36. The blockage ratio is the ratio of the capsule's cross-sectional area to the tube's cross-sectional area. The formula for calculating BR is denoted by Eq. (1)

$$BR = \frac{\text{Cross-sectional area of pod}}{\text{Cross-sectional area of tube}} = \frac{d_{pod}^2}{d_{\text{tube}}^2} \tag{1}$$

Mathematical Model

In the problems of compressible fluid, the governing equations consist of conservation of mass, Navier-Stokes, and energy equation. The continuity equation can be written as follows:

$$\frac{\partial \rho}{\partial t} + \frac{\partial (\rho u_i)}{\partial x_i} = 0 \tag{2}$$

The equation of momentum and energy, respectively, can be written as:

$$\frac{\partial (\rho u_i)}{\partial t} + \frac{\partial (\rho u_i u_j)}{\partial x_j} = \frac{\partial P}{\partial x_j} + \frac{\partial}{\partial x_j}\left[\mu\left(\frac{\partial u_i}{\partial x_j} + \frac{\partial u_j}{\partial x_j} - \frac{2}{3}\delta_{ij}\frac{\partial u_m}{\partial x_m}\right)\right]\frac{\partial}{\partial x_j}\left(-\rho u_i u_j\right) \tag{3}$$

$$\frac{\partial (\rho E)}{\partial t} + \frac{\partial (u_j (\rho E + P))}{\partial x_j} = \frac{\partial P}{\partial x_j}\left(k_{eff}\frac{\partial T}{\partial x_j}\right) + \frac{\partial}{\partial x_j}\left[u_i \mu_{eff}\left(\frac{\partial u_i}{\partial x_j} + \frac{\partial u_j}{\partial x_j} - \frac{2}{3}\delta_{ij}\frac{\partial u_m}{\partial x_m}\right)\right] \tag{4}$$

Here, ρ is the fluid's density, u is the fluid's velocity, p is the fluid pressure, and μ is the fluid's viscosity. In the energy equation, E is the fluid's specific internal energy, k_{eff} is effective thermal conductivity, and μ_{eff} is effective dynamic viscosity. The flow separation events are successfully predicted by the solver using an SST turbulence model. The SST k- ω transport equation is combined with other transport equations in transition SST models. The following are some examples of the equations [14]:

$$\frac{\partial(\rho k)}{\partial t}+\frac{\partial\left(\rho U_j k\right)}{\partial x_j}=\frac{\partial}{\partial x_j}\left[\left(\mu+\frac{\mu_t}{\sigma_k}\right)\frac{\partial k}{\partial x_j}\right]+\gamma_{eff}\tilde{G}_k-min\left(max\left(\gamma_{eff},0.1\right)Y_k+S_k\right) \quad (5)$$

where,

$$\gamma_{eff}=max\left(\gamma,\gamma_{sep}\right) \quad (6)$$

$$\gamma_{\text{sep}}=min\left(C_{s1}max\left[\left(\frac{Re_v}{3.235\text{Re}_{\theta c}}\right)-1{,}0\right]F_{\text{reattach}},2\right)F_{\theta t} \quad (7)$$

$$\frac{\partial(\rho\gamma)}{\partial t}+\frac{\partial\left(\rho U_j\gamma\right)}{\partial x_j}=P_{\gamma1}-E_{\gamma1}+P_{\gamma2}-E_{\gamma2}+\frac{\partial}{\partial x_j}\left[\left(\mu+\frac{\mu_t}{\sigma_\gamma}\right)\frac{\partial\gamma}{\partial x_j}\right]. \quad (8)$$

For the SST model, $\tilde{G}_k$ is the production term and Y_k is destruction term. These equations result in a more realistic prediction of boundary layer characteristics, which are crucial in Hyperloop systems that operate at transonic speeds.

Computational Grid

A 2-dimensional computational domain was specified using a hexahedral mesh. To adjust the mesh to the geometry of the capsule's front and back, the unstructured mesh was produced in the regions adjacent to the capsule's ends. Both the capsule's wall and the tunnel's walls were inflated with finer layers of gas. Figure 2 depicts the mesh generated in the capsule's front and rear regions. After meshing, the mesh metric was also tested. The quality of the geometry elements is 0.87489, skewness is 1.4581e-3, and orthogonal quality is 0.99979. These values were very close to what was expected from a CFD simulation of these parameters. The mesh metric table is given below in Table 1.

Table 1. Mesh metric

Sl. No.	Parameters name	Average value
1.	Element quality	0.87489
2.	Aspect ratio	4.4237
3.	Skewness	1.4581e-003
4.	Orthogonal quality	0.99979

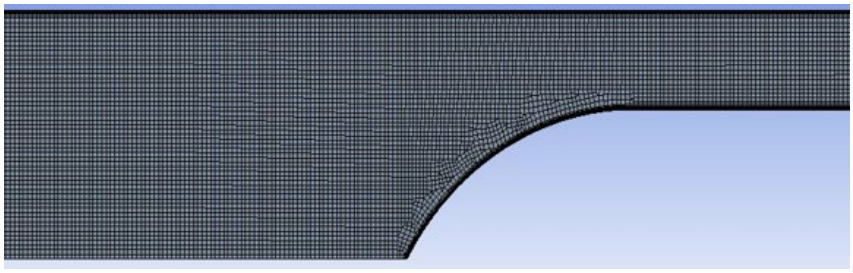

(a)

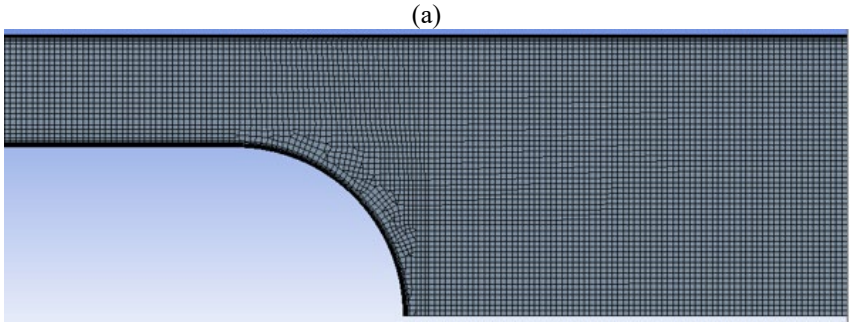

(b)

Figure 2. Mesh at the (a) front and (b) rear of the capsule

For the grid independence test, the highest velocity of 350 m/s, BR 0.25, and pressure of 101.325Pa were taken into account. Though three types of mesh have been created consisting of a course (Mesh 1), fine (Mesh 2), and finer (Mesh 3). Mesh 2 is applied to run all the simulations with around 1 million cells. The obtained results for each case are listed in Table 1 where total drag, number of cells, and maximum pressures with a relative error are demonstrated.

Table 2. Grid independence test value

Case	Number of cells	Total drag, D_T (N) (Relative error)	Highest pressure, P_{max} (Pa)
Mesh 1	0.6 million	1086.43 (0.45%)	235.39 (0.0170%)
Mesh 2	1.0 million	1081.48 (0.11%)	235.36 0.00428%
Mesh 3	1.5 million	1080.28	235.35

The grid independence curve has been plotted in Figure 3, which is identical to the total drag column in Table 1. As can be seen, the total drag for Mesh 3 (1.5 million cells) isn't all that different from mesh (1 million cells). There was only a 0.11% difference in relative error between these two examples. Furthermore, there was only a 0.00428% discrepancy between these two cases in the relative error of the highest pressure. Based on the above-mentioned midget difference, we have concluded Mesh 2 (element size of 3×10^{-2} m) would be used in all simulations instead of finer mesh. The calculations for Mesh 2 were performed using a windows PC consisting of an Intel Core i5 10^{th} generation(8 core) processor of 4.80 GHz and 16-gigabyte ram. It took almost 5-7 hours to converge and stable results for most cases.

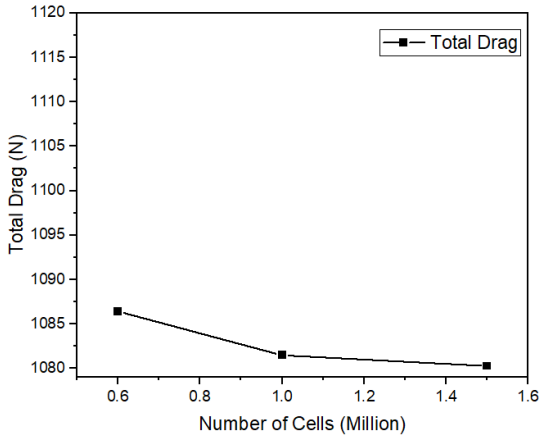

Figure 3. Grid independence curve

Wall Y+ values

The wall y+ values show the degree of development of the viscous boundary layer. This was accomplished by incorporating an inflating layer within the tube and capsule walls. In every instance, the y+ values of the walls were kept below 1. Figure 4 depicts a sample curve of y+ values for both the pod and the moving wall. The maximum value of y+ is recorded at 200 m/s and 101,325 Pa at the capsule's tip and back. Except for that, the y+ readings along the capsule and moving wall were extremely low, i.e. below 0.15.

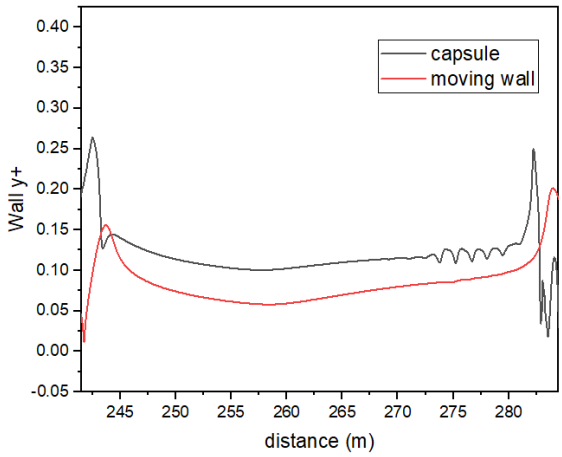

Figure 4. Variation of Wall y+ along the surface of the capsule and moving wall of the tunnel

Validation

A domain with semicircular capsule ends was established to validate the model. The velocity, pressure and BR were determined to be 350 m/s, 101.31 bar, and 0.36 correspondingly. The dimensions of the model are comparable to the analysis conducted by Oh et al. [14]. Conditions for the validation analysis were identical to those of the reference research. For this approach, a 2D axisymmetric steady analysis was performed. The present result is compared to the

reference results. Figure 5 illustrates the validation curve; it demonstrates a comparable trend for drag force between the two assessments, indicating a high level of acceptability. Thus, considering the validation result, our chosen numerical method is appropriate for simulating the intended analysis. In our study, the CFD simulation was performed for the elliptical-shaped front and semicircular-shaped rear of the capsule. The boundary condition was selected as pressure-far-field for both the inlet and outlet, as there is no chance of reflection at the boundary in this boundary condition. Apart from that, all the conditions remain almost identical to the reference study.

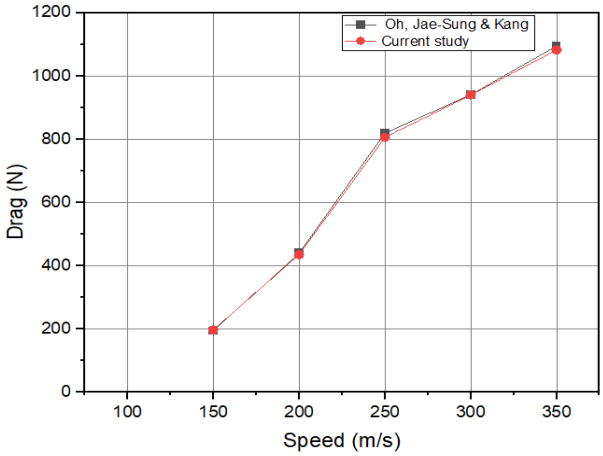

Figure 5. Validation and comparison with data obtained by Oh et al. [14] of total drag when both ends of the capsule are semicircular

RESULTS AND DISCUSSION

Effect of Capsule Speed and Tunnel Pressure

The capsule's aerodynamic drag has been investigated and plotted in Figure 6 against the increasing speed at various tunnel pressures where total drag consists of pressure drag and friction drag. It is shown that total drag for all tunnel pressures increases with increasing capsule velocity because ideal gas density increases with increasing pressure. As atmospheric pressure increases based on our reference pressure from 101.325 Pa to 1013.25Pa, air density follows an increasing trend. Due to the increased density, the capsule must contend with a larger resistance to its forward motion. Consequently, the value of total drag increases with increasing pressure at constant velocity.

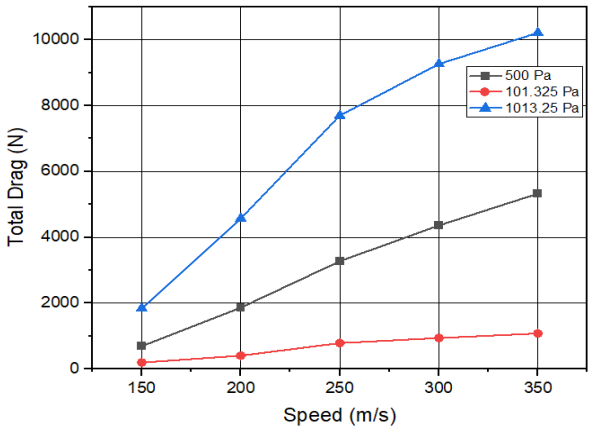

Figure 6. Total drag vs speed

From Figure 6, the total drag value showed a static increment with speed proliferation, and it becomes steady after 300 m/s, but at 500 Pa, drag followed a gradually increasing trend up to 350 m/s speed and presented a straight slope compared to 101.325 Pa. Drag for 1013.25 Pa exhibit a rapid surge after 250 m/s speed though before it was gradual like the other two lines as explained earlier. This is because, at 250 m/s, shock waves appear at the capsule's rear for all pressures. A combination of expansion and reverberation waves creates these shockwaves. A low-pressure area is created behind the capsule as a result of a wavy region. Again, the difference in pressure between the tip and the back of the capsule grows. As a result, the total amount of drag increases as the vehicle's speed increases. Semicircular heads and oval heads were compared in terms of their total drag. Elliptical heads performed better in most cases because they produced less drag. Semicircular-headed capsules, on the other hand, performed better at high speeds (200 m/s and 250 m/s). There were different flow patterns formed as a result. The outlet boundary conditions may also be to blame for this. It was decided to use the pressure-outlet condition in the reference. In this case, there is possibility of pressure

reverberation interacting with the pod's surrounding flow field [21]. However, we used Pressure Far-Field conditions, in which no pressure reflection can occur at the boundary for both the inlet and the outlet conditions.

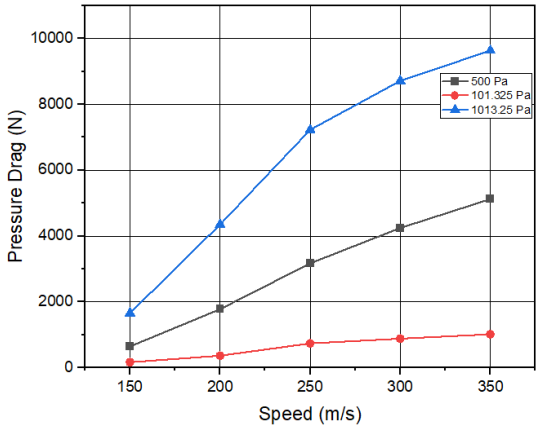

Figure 7. Pressure drag vs speed

The effect of capsule pressure and velocity is shown in Figure 7. The pressure difference between the capsule's tip and tail determines the pressure drag. The pressure differential between the capsule's tip and tail expands at a consistent rate as velocity increases. The pressure differential increases at the same rate as the tunnel pressure rises. Because pressure drag accounts for the bulk of total drag, the curves in Figure 6 and Figure 7 have almost similar tendencies. The impact of capsule velocity and pressure on frictional drag differs from pressure drag. It has a minimal effect on total drag as its value is much lower than pressure drag. For every tunnel pressure, there is a rapid increase in frictional drag after the capsule reaches 200 meters per second, see Figure 8. This occurs because after 200 m/s the turbulence strength on the capsule's wall becomes significant [13].

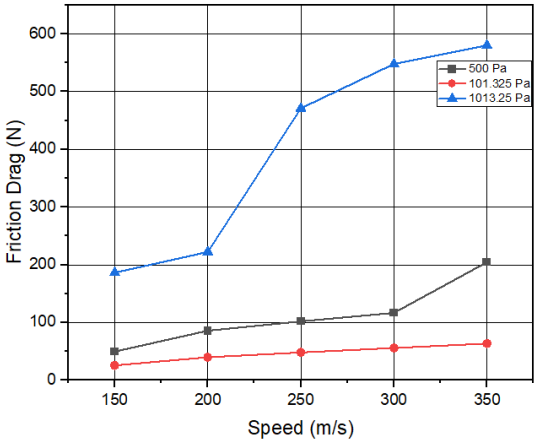

Figure 8. Friction drag vs speed

Mach Number and Pressure Analysis

A sample Mach number distribution and pressure distribution are given below for 101.325 Pa in a Hyperloop tunnel is illustrated in Figure 9 and Figure 10. Figure 9(c) shows the Mach number distribution near the capsule. There is a sudden increase in the Mach number at the real zone of the pod. A noticeable increase in pressure in Figure 10 is also identified from 200 m/s to 250 m/s. At these velocities, the choking becomes severe due to the formation of shockwaves. It can be noted that, although there is an increase in pressure and Mach number from 150 m/s to 200 m/s, the pressure value at the rear of the capsule exhibited a significant pressure drop after 200 m/s due to the formation of a shockwave.

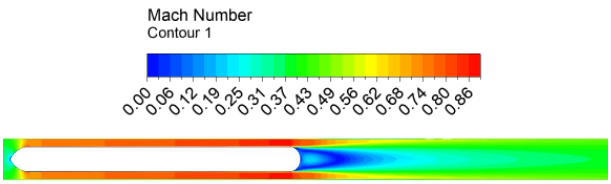

(a) 150 m/s

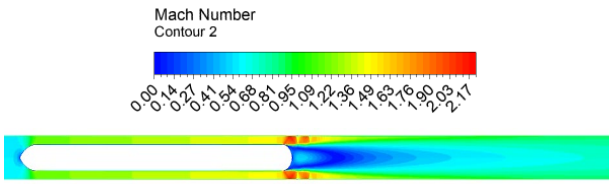

(b) 200 m/s

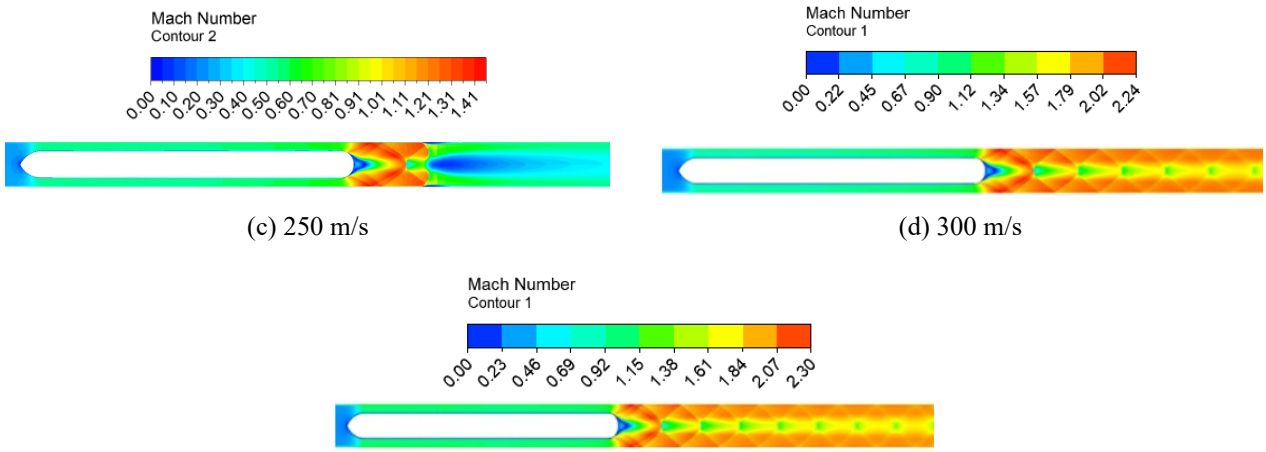

(c) 250 m/s (d) 300 m/s

(e) 350 m/s

Figure 9. Mach number contour for different speeds at a pressure of 1013.25 Pa

Figure 10 shows that the pressure differential between the front and rear of the capsule increases as the temperature rises. Total drag and pressure drag force were also boosted by this change in the ratio of pressure to total drag. Despite this, the capsule's pressure differential remains unchanged at speeds of 150 and 200 m/s. Pressure drag and frictional drag were not significantly affected. The pressure differential between the capsule's two ends increased significantly after 250 m/s. This was caused by shockwaves forming at the back of the capsule. A low-pressure zone is formed behind the capsule as a result. After that, there was a significant shift in the amount of pressure. For this reason, total drag and pressure drag increased significantly after 250 m/s, as explained earlier in Figure 6 and Figure 7, respectively.

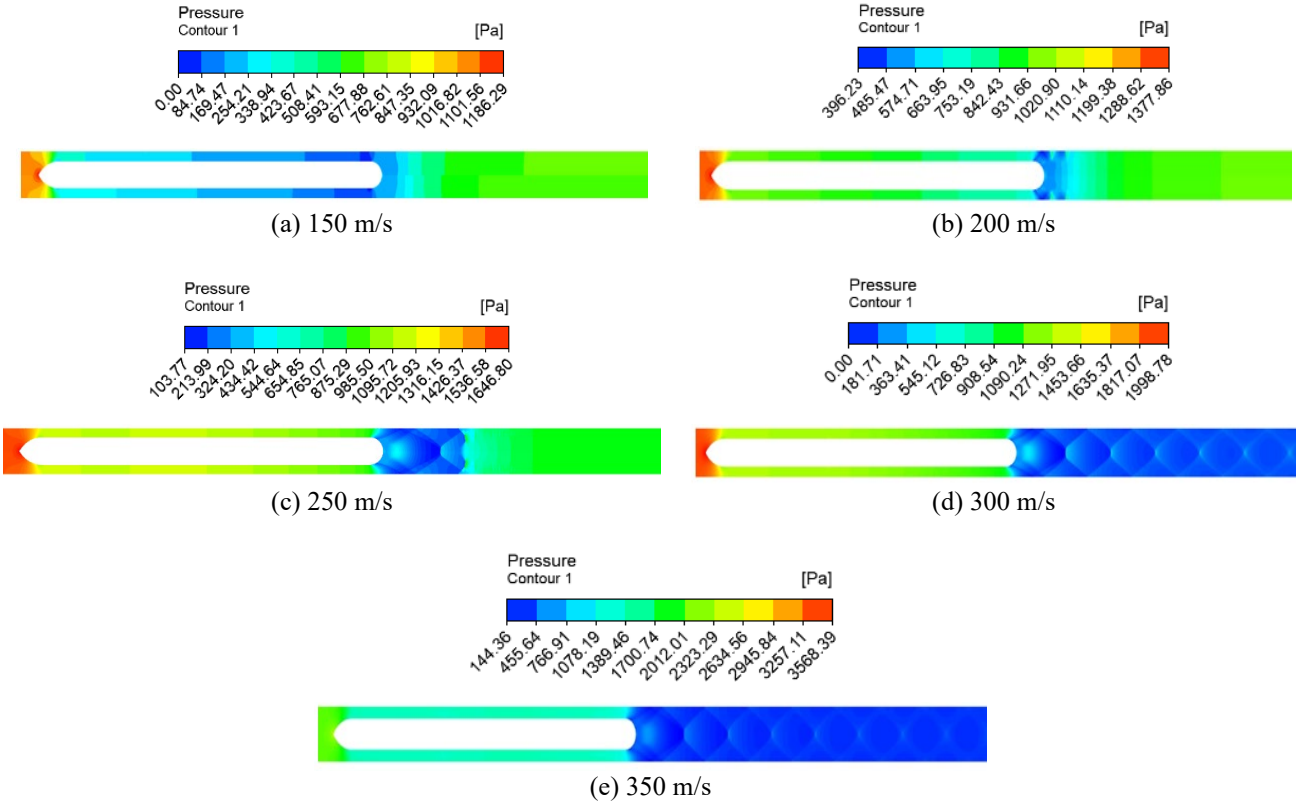

(a) 150 m/s (b) 200 m/s

(c) 250 m/s (d) 300 m/s

(e) 350 m/s

Figure 10. Pressure contour for different speeds at a pressure of 1013.25 Pa

Figure 11 illustrates the effect of tunnel pressure on Mach number contour and pressure distribution. All three pressure conditions were depicted in the sample contours for 200 m/s shown here. Pressure and Mach numbers in all zones increase as the tunnel pressure rises at the same speed. Additionally, as tunnel pressure rises, so does the pressure differential between the capsule ends. As a result, even at the same speed, the tunnel pressure increases the overall drag and friction drag—Figure 6 and Figure 7 show this trend. There was a consistent pattern regardless of the speed of the vehicle.

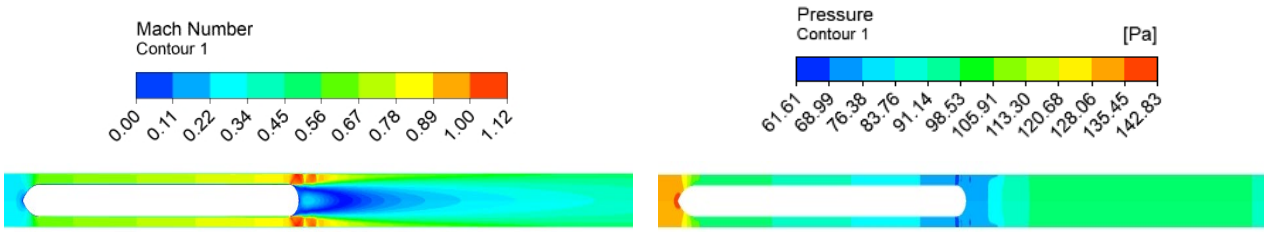

(a) 101.325 Pa

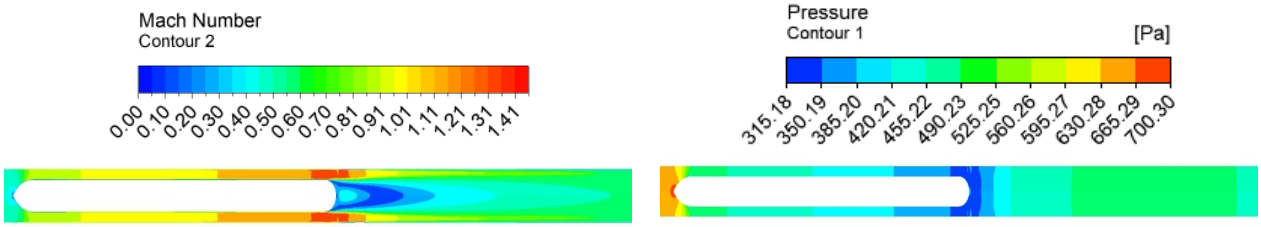

(b) 500 Pa

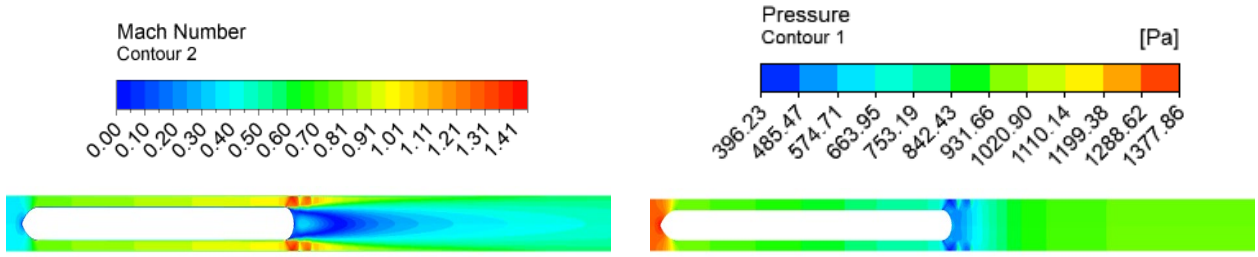

(c) 1013.25 Pa

Figure 11. Mach number contour and pressure contour at 200 m/s

Wave Propagation Analysis

A Hyperloop system's flow resembles that of a converging-diverging duct. At high speeds, choking and shock waves are present. At 250 m/s, the shock wave begins to appear. The Hyperloop's fundamental flow fields can be separated into three areas comprising the piston, choked, and nozzle regions which are illustrated in Figure 12. In the region surrounding the piston, the air has accumulated. For this reason, the pressure in this location is considerably high. The obstructed zone is located in the space between the capsule wall and the tunnel wall. This region's pressure lowers due to choking. There are expansion waves and shock waves created in the nozzle region. Consequently, a low-pressure zone forms in this location. If we run a temperature and pressure lines along the tunnel, we can observe these locations accurately.

Transition, throat, and nozzle zones can be distinguished in the choked region. Figure 12(b) shows the transition zone between the piston and throat regions. As the Hyperloop travels through the tunnel, a portion of the air from the throat zone flows into nozzle zone. As the throat chokes, the transition zone fills up with air. Consequently, the transition and piston zones are filled with air. Prandtl-Meyer flow can be seen in the nozzle zone. The temperature and pressure decrease before the wake region is caused by an expansion wave generated downstream and reflected in the tunnel wall. Again, a bow shock is formed before the capsule, which is reflected from the head of the capsule and the wall of the tunnel. The arch of the bow shock wave dwindled and became a normal shock wave over time.

After the nozzle region, the wake region appears. The wake region has a complex flow structure composed of expansion wave, shock wave, and expansion wave-expansion wave interaction. The expansion wave is formed at the nozzle reflected off the tunnel wall and interacts with each other at the center of the tunnel; it creates a series of rhomboidal waves in Figure 13. Higher capsule speeds of 250 m/s, 300 m/s and 350 m/s generate shock waves in the wake region. This region features a complex flow pattern due to the presence of shock waves, expansion waves, and wave interaction. Tunnel walls reflect expansion waves, which intersect near the centerline. The outcome is the formation of a rhomboid wave structure. Figure 13(a) illustrates a sequence of various types of waves. After the tunnel wall has reflected the expansion wave, the pressure begins to climb. Following this, the reflected waves interact at the centerline, and the wave pressure begins to decrease. The pressure rapidly decreased as the number of rhomboidal shock waves added to the series in the wake region increased. This can be detected by observing the oscillation of waves along line 1 drawn 0.3D from the centerline in Figure 13(b).

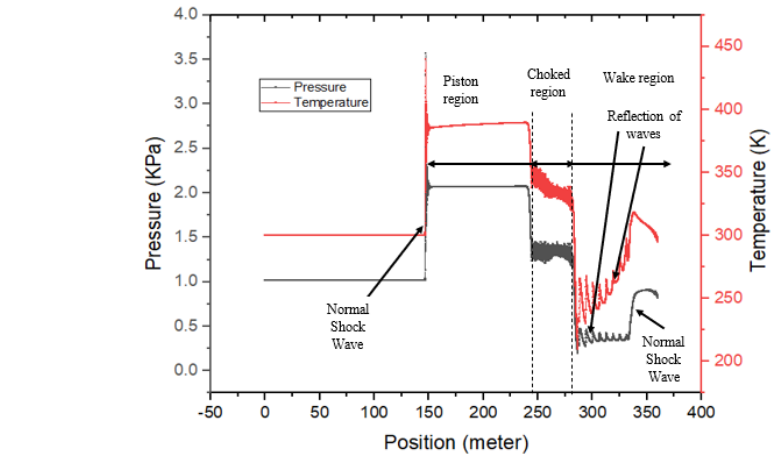

(a)

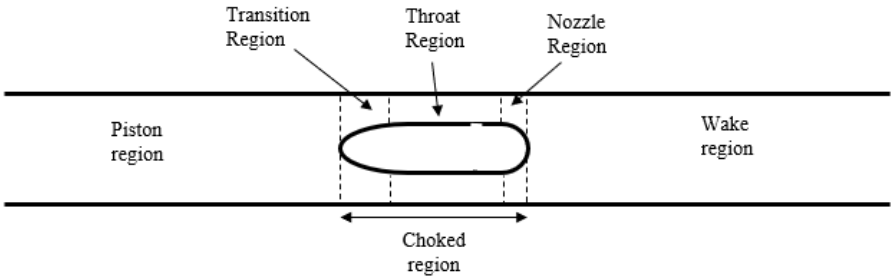

(b)

Figure 12. (a) Pressure and temperature distribution along the tunnel wall in different regions and (b) partition diagram of the flow field

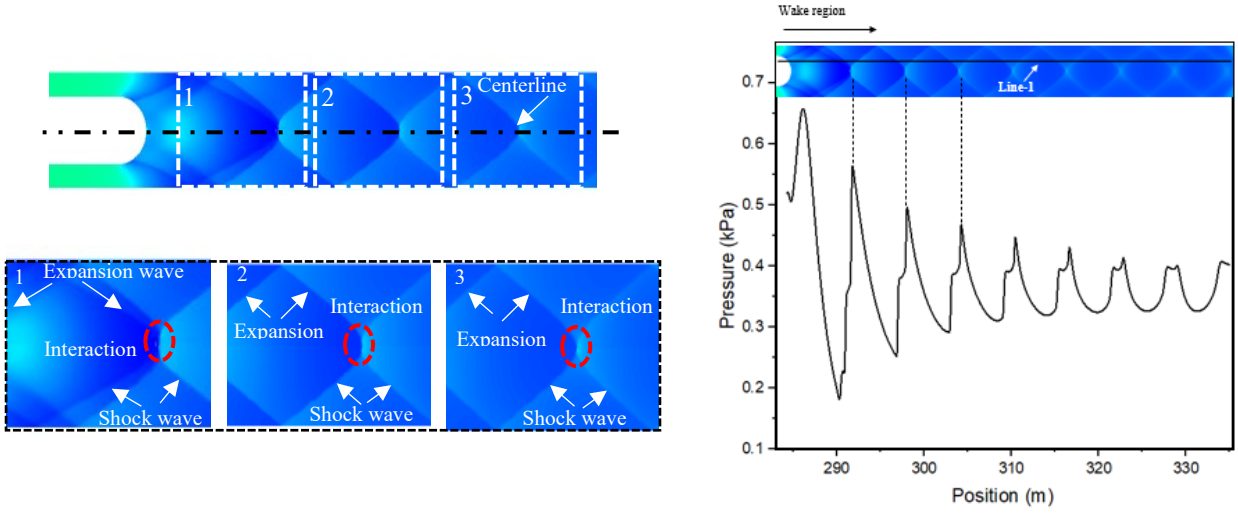

(a) (b)

Figure 13. (a) Wave structure at the wake region (BR 0.36, P= 1013.25 Pa, 350 m/s), and (b) pressure distribution along Line-1 (0.3D from the centerline of the tube) in the wake region

CONCLUSIONS

In this project, the aerodynamic drag at different tunnel pressures (101.325 Pa, 500 Pa, and 1013.25 Pa) and capsule speeds (150 m/s, 200 m/s, 250 m/s, 300 m/s and 350 m/s) were determined by using ANSYS fluent 18.1. The shock waves found at high speeds were also analyzed. The findings of this investigation are:

i. Aerodynamic drags are reduced when the elliptic head is used instead of the semicircular head. The shapes create a flow field where the pressure difference between the capsule head and tail decreases in most cases for the same evacuated pressure and capsule speed. At 101.325 Pa, 500 Pa, and 1013.25 Pa tunnel pressure, the minimum reductions of total drag were 0.24%, 9.8%, and 0.11%, respectively, and the maximum total drag reductions were 7.7%, 16%, and 11%, respectively comparing with the capsule with semicircular ends described in Oh et al. [14].

ii. As the speed increases, the total drag also increases. The viscous interaction with the wall of the pod increases with speed. So, the friction drag also increases with speed. After 200 m/s, there was a rapid change in friction drag due to the increase in turbulence intensity.

iii. As the pressure increases, the density also increases according to the ideal gas law. So, at higher pressure, the capsule faces more obstructive force at the same speed and the pressure difference between the capsule head and rear increases. So, the pressure drag also increases.

iv. At high speed, a series of rhomboid shape shock waves appear. In choked conditions, there is accumulated air in front of the capsule, and a low-pressure zone is created behind the capsule due to the formation of shock waves in the wake region.

v. At high speed, when the flow is choked, the temperature and pressure are maximum in the accumulated region. Then they started to fall in the choked region, and they were minimum in the wake region due to the formation of expansion waves, shock waves, and their interaction.

ACKNOWLEDGEMENT

We thank all of the educators and staff at Khulna University of Engineering and Technology's Department of Mechanical Engineering for their assistance in completing the mission.

REFERENCES

[1] D. Oster, "Evacuated tube transport," Google Patents 5,950,543, 1999.

[2] F. C. Barbosa, "Hyperloop concept technological and operational review: The potential to fill rail niche markets," in *ASME/IEEE Joint Rail Conference*, 2020, p. V001T03A004.

[3] Z. Deng, W. Zhang, J. Zheng, B. Wang, Y. Ren *et al.*, "A high-temperature superconducting maglev-evacuated tube transport (HTS Maglev-ETT) test system," *IEEE Transactions on Applied Superconductivity,* vol. 27, no. 6, pp. 1-8, 2017.

[4] A. S. Abdelrahman, J. Sayeed, and M. Z. Youssef, "Hyperloop transportation system: analysis, design, control, and implementation," *IEEE Transactions on Industrial Electronics,* vol. 65, no. 9, pp. 7427-7436, 2017.

[5] E. Musk, "Hyperloop alpha document," SpaceX: Hawthorne, CA, USA, 2003.

[6] J. Niu, Y. Sui, Q. Yu, X. Cao, and Y. Yuan, "Aerodynamics of railway train/tunnel system: A review of recent research," *Energy and Built Environment,* vol. 1, no. 4, pp. 351-375, 2020.

[7] Y. Zhang, "Numerical simulation and analysis of aerodynamic drag on a subsonic train in evacuated tube transportation," *Journal of Modern Transportation,* vol. 20, no. 1, pp. 44-48, 2012.

[8] H. Kang, Y. Jin, H. Kwon, and K. Kim, "A study on the aerodynamic drag of transonic vehicle in evacuated tube using computational fluid dynamics," *International Journal of Aeronautical and Space Sciences,* vol. 18, no. 4, pp. 614-622, 2017.

[9] J. Braun, J. Sousa, and C. Pekardan, "Aerodynamic design and analysis of the hyperloop," *AIAA Journal,* vol. 55, no. 12, pp. 4053-4060, 2017.

[10] Y. Yang, H. Wang, M. Benedict, and D. Coleman, "Aerodynamic simulation of high-speed capsule in the Hyperloop system," In Proc. of 35th AIAA Applied Aerodynamics Conference, 2017, p. 3741.

[11] M. M. Opgenoord and P. C. Caplan, "Aerodynamic design of the Hyperloop concept," *AIAA Journal,* vol. 56, no. 11, pp. 4261-4270, 2018.

[12] F. Wong, "Aerodynamic design and optimization of a hyperloop vehicle," MSc. Thesis, Delft University of Technology, Delft, 2018.

[13] Y. K. Singh and K. Mehran, "Numerical analysis for aerodynamic behaviour of hyperloop pods," *Preprints* 2019, 2019120101, 2019.

[14] J.-S. Oh, T. Kang , S. Ham, K.-S. Lee, Y.-J. Jang *et al.*, "Numerical analysis of aerodynamic characteristics of hyperloop system," *Energies,* vol. 12, no. 3, p. 518, 2019.

[15] T. Désert, T. Jardin, H. Bézard, and J.-M. Moschetta, "Numerical predictions of low Reynolds number compressible aerodynamics," *Aerospace Science and Technology,* vol. 92, pp. 211-223, 2019.

[16] N. Nick and Y. Sato, "Computational fluid dynamics simulation of Hyperloop pod predicting laminar–turbulent transition," *Railway Engineering Science,* vol. 28, no. 1, pp. 97-111, 2020.

[17] V. Fomin and D. Nalivaychenko, "Questions of aerodynamics the vacuum-levitation transport system," *AIP Conference Proceedings*, vol. 1893, no. 1, p. 020001, 2017.

[18] F. Lluesma-Rodríguez, T. González, and S. Hoyas, "CFD simulation of a hyperloop capsule inside a closed environment," *Results in Engineering,* vol. 9, p. 100196, 2021.

[19] Y. Sui, J. Niu, Q. Yu, Y. Yuan, X. Cao, and X. Yang, "Numerical analysis of the aerothermodynamic behavior of a Hyperloop in choked flow," *Energy,* vol. 237, p. 121427, 2021.

[20] F. Lluesma-Rodríguez, T. González, and S. Hoyas, "CFD simulation of a hyperloop capsule inside a low-pressure environment using an aerodynamic compressor as propulsion and drag reduction method," *Applied Sciences,* vol. 11, no. 9, p. 3934, 2021.

[21] T. T. G. Le, K. S. Jang, K.-S. Lee, and J. Ryu, "Numerical investigation of aerodynamic drag and pressure waves in hyperloop systems," *Mathematics,* vol. 8, no. 11, p. 1973, 2020.

[22] T.-K. Kim, K.-H. Kim, and H.-B. Kwon, "Aerodynamic characteristics of a tube train," *Journal of wind engineering and industrial aerodynamics,* vol. 99, no. 12, pp. 1187-1196, 2011.

[23] T. T. G. Le, J. Kim, K. S. Jang, K.-S. Lee, and J. Ryu, "Numerical study on the influence of the nose and tail shape on the aerodynamic characteristics of a Hyperloop pod," *Aerospace Science and Technology,* vol. 121, p. 107362, 2022.

[24] Q. Yu, X. Yang, J. Niu, Y. Sui, Y. Du, and Y. Yuan, "Theoretical and numerical study of choking mechanism of fluid flow in Hyperloop system," *Aerospace Science and Technology,* vol. 121, p. 107367, 2022.

[25] H. Kim and S. Oh, "Shape optimization of a hyperloop pod's head and tail using a multi-resolution morphing method," *International Journal of Mechanical Sciences,* vol. 223, p. 107227, 2022.

[26] H. Kim and S. Oh, "Shape optimization with a flattening-based morphing method," *Applied Sciences,* vol. 12, no. 13, p. 6565, 2022.
[27] T. T. G. Le, J. Kim, K. S. Jang, K.-S. Lee, and J. Ryu, "Numerical study of unsteady compressible flow induced by multiple pods operating in the Hyperloop system," *Journal of Wind Engineering and Industrial Aerodynamics,* vol. 226, p. 105024, 2022.
[28] Z. Zhou, C. Xia, X. Du, X. Shan, and Z. Yang, "Impact of the isentropic and Kantrowitz limits on the aerodynamics of an evacuated tube transportation system," *Physics of Fluids,* vol. 34, no. 6, p. 066103, 2022.
[29] K. S. Jang, T. T. G. Le, J. Kim, K.-S. Lee, and J. Ryu, "Effects of compressible flow phenomena on aerodynamic characteristics in Hyperloop system," *Aerospace Science and Technology,* vol. 117, p. 106970, 2021.
[30] T. Yoon, S. Lee, J. Hwang, and D. Lee, "Prediction and validation on the sonic boom by a high-speed train entering a tunnel," *Journal of Sound and vibration,* vol. 247, no. 2, pp. 195-211, 2001.
[31] J. Zonglin, K. Matsuoka, A. Sasoh, and K. Takayama, "Numerical and experimental investigation of wave dynamic processes in high-speed train/tunnels," *Acta Mechanica Sinica,* vol. 18, no. 3, pp. 209-226, 2002.